JOURNAL OF GEOPHYSICAL RESEARCH, VOL. 105, NO. B6, PAGES 13,859–13,874, JUNE 10, 2000

Three-dimensional seismic velocity structure of the San Francisco Bay area

J. A. Hole,[1] T. M. Brocher,[2] S. L. Klemperer,[3] T. Parsons,[2]
H. M. Benz,[4] and K. P. Furlong[5]

Abstract. Seismic travel times from the northern California earthquake catalogue and from the 1991 Bay Area Seismic Imaging Experiment (BASIX) refraction survey were used to obtain a three-dimensional model of the seismic velocity structure of the San Francisco Bay area. Nonlinear tomography was used to simultaneously invert for both velocity and hypocenters. The new hypocenter inversion algorithm uses finite difference travel times and is an extension of an existing velocity tomography algorithm. Numerous inversions were performed with different parameters to test the reliability of the resulting velocity model. Most hypocenters were relocated <2 km from their catalogue locations. Large lateral velocity variations at shallow (<4 km) depth correlate with known surface geology, including low-velocity Cenozoic sedimentary basins, high-velocity Cenozoic volcanic rocks, and outcrop patterns of the major Mesozoic geologic terranes. Salinian arc rocks have higher velocities than the Franciscan melange, which in turn are faster than Great Valley Sequence forearc rocks. The thickess of low-velocity sediment is defined, including >12 km under the Sacramento River Delta, 6 km beneath Livermore Valley, 5 km beneath the Santa Clara Valley, and 4 km beneath eastern San Pablo Bay. The Great Valley Sequence east of San Francisco Bay is 4-6 km thick. A relatively high velocity body exists in the upper 10 km beneath the Sonoma volcanic field, but no evidence for a large intrusion or magma chamber exists in the crust under The Geysers or the Clear Lake volcanic center. Lateral velocity contrasts indicate that the major strike-slip faults extend subvertically beneath their surface locations through most of the crust. Strong lateral velocity contrasts of 0.3-0.6 km/s are observed across the San Andreas Fault in the middle crust and across the Hayward, Rogers Creek, Calaveras, and Greenville Faults at shallow depth. Weaker velocity contrasts (0.1-0.3 km/s) exist across the San Andreas, Hayward, and Rogers Creek Faults at all other depths. Low spatial resolution evidence in the lower crust suggests that the top of high-velocity mafic rocks gets deeper from west to east and may be offset under the major faults. The data suggest that the major strike-slip faults extend subvertically through the middle and perhaps the lower crust and juxtapose differing lithology due to accumulated strike-slip motion. The extent and physical properties of the major geologic units as constrained by the model should be used to improve studies of seismicity, strong ground motion, and regional stress.

1. Introduction

The relative plate motion between the North American and Pacific plates in the San Francisco Bay (SFBay) area is spread over a broad zone ~100 km wide, encompassing several major active faults, including the San Gregorio, San Andreas, Hayward, Rogers Creek, Calaveras, Green Valley, and Greenville Faults (Figure 1) [*Jennings*, 1994]. All of these faults have the potential to generate major earthquakes in an urban area. Abundant seismicity in the region is recorded by numerous seismographs of the Northern California Seismic Network (NCSN), maintained by the U.S. Geological Survey (USGS) (Figure 2). In addition, an air gun source used in the 1991 Bay Area Seismic Imaging Experiment (BASIX) was recorded at both temporary and NCSN seismograph sites throughout the SFBay area (Figure 2) [*Brocher et al.*, 1994]. Combined, these data sets provide excellent three-dimensional (3-D) ray coverage of the upper crust. This paper presents a 3-D seismic velocity model of the SFBay area derived from tomographic inversion of the earthquake and air gun first-arrival travel time data.

The geology of the upper crust of the SFBay area (Figure 1) consists primarily of a Mesozoic arc (Sierra Nevada and Salinian terrane), forearc basin (Great Valley Sequence) and accretionary prism (Franciscan terrane) [*Jennings*, 1977; *Page et al.*, 1998]. West of the San Andreas Fault, granitic rocks of the Salinian terrane have been displaced to the northwest from southern California by strike-slip motion on the fault. Franciscan rocks, consisting of a Mesozoic through Eocene melange of deep-sea graywackes and shales in an accretionary complex, form most of the upper crust in the SFBay area east of the San Andreas Fault (Figure 1). Ophiolites exist in the Franciscan terrane in the SFBay area but are volumetrically

[1]Department of Geological Sciences, Virginia Polytechnic Institute and State University, Blacksburg.
[2]U.S. Geological Survey, Menlo Park, California.
[3]Department of Geophysics, Stanford University, Stanford, California.
[4]U.S. Geological Survey, Lakewood, Colorado.
[5]Department of Geosciences, Pennsylvania State University, University Park.

Paper number 2000JB900083.
0148-0227/00/2000JB900083$09.00

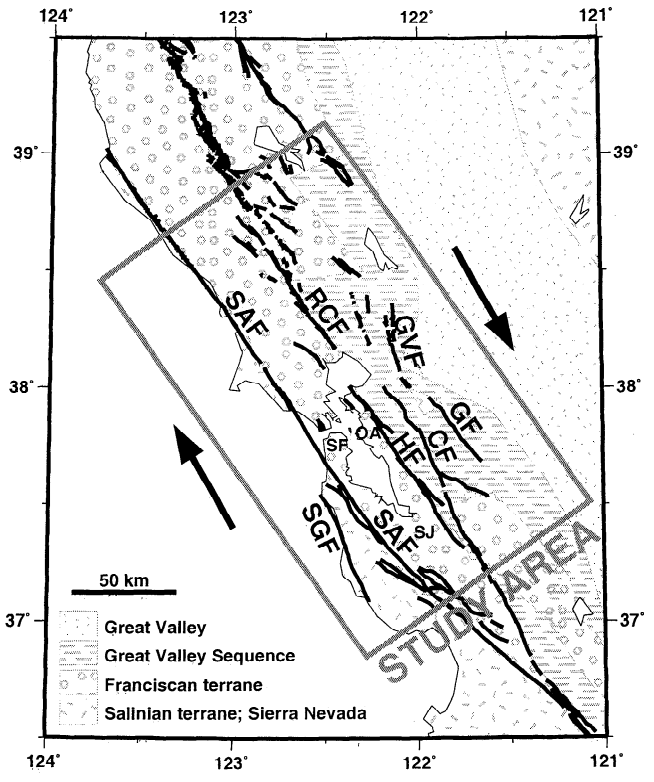

Figure 1. Map of the San Francisco Bay area indicating the study area for the 3-D velocity model. Major faults indicated by thick lines are SGF, San Gregorio; SAF, San Andreas; HF, Hayward; RCF, Rogers Creek; CF, Calaveras; GVF, Green Valley; GF, Greenville. Arrows show the direction of relative plate motion distributed across the region. Simplified geology of the upper crust is shown in gray [*Page et al.*, 1998]. Cities are SF, San Francisco; OA, Oakland; SJ, San Jose.

minor. The melange is relatively homogeneous at the seismic wavelengths typical of earthquake and crustal refraction studies. Folded and thrusted shallow marine sandstones and shales of the Great Valley Sequence overlie the Franciscan terrane in the upper crust east of the Hayward Fault.

The major Mesozoic crustal units are locally covered by younger rocks. Cenozoic volcanic rocks of the Clear Lake and Sonoma fields outcrop north and east of the Rogers Creek Fault. A thin cover of Cenozoic sediments covers many parts of the region, and locally thicker basins exist at several locations. The Great Valley to the east contains a thick sequence of Jurassic through Quaternary sediments.

Three-dimensional seismic velocity models have been published for portions of the study area (Figure 2), but no model exists that focuses on the entire SFBay region. Several tomography studies inverted aftershock data from the 1989 Loma Prieta earthquake to obtain structure overlapping the southwestern corner of the study area (Figure 2) [e.g., *Foxall et al.*, 1993; *Thurber et al.*, 1995; *Eberhart-Phillips and Michael*, 1998]. Tomography has also been performed using aftershocks from the 1984 Morgan Hill earthquake in the south of the study area [*Michael*, 1988]. Abundant microseismicity associated with geothermal activity made possible detailed velocity models at The Geysers in the far northern end of the study area (Figure 2) [e.g., *Romero et al.*, 1995; *Julian et al.*, 1996]. Regional seismicity was used to study the upper crust surrounding The Geysers [*Eberhart-Phillips*, 1986; *Stanley et al.*, 1998]. The model of *Stanley et al.* [1998] overlapped the northern third of our study area, but the interpretation was focused on structure near The Geysers. Explosions and earthquakes were used to obtain velocity structure in the upper crust on the northern San Francisco Peninsula (Figure 2) [*Parsons and Zoback*, 1997].

Several refraction surveys provide two-dimensional constraints on the seismic velocity structure of the crust (Figure 2). Sparsely sampled 1967 refraction lines south of SFBay [*Walter and Mooney*, 1982] and 1976 lines north of the bay [*Warren*, 1981] provide first-order information on either side of the major faults. An offshore-onshore 1990 survey constrains structure at the latitude of the Loma Prieta earthquake [*Page and Brocher*, 1993]. The BASIX reflection-refraction survey produced crustal velocity models centered in the study area along SFBay and across the San Andreas Fault at San Francisco (Figure 2) [*Holbrook et al.*, 1996]. A parallel line was obtained along the San Francisco Peninsula [*Catchings and Kohler*, 1996]. A refraction survey of the upper 6-8 km of the crust was acquired across Livermore Valley [*Meltzer et al.*, 1987].

The earthquake tomography models and refraction profiles indicate that first-order differences in seismic velocity exist between the major Mesozoic units. Rocks of the Salinian terrane are faster than those of the Franciscan terrane, which in turn are faster than the Great Valley and younger sediments. These velocity contrasts have been used in some of the above studies to identify the subsurface locations of faults. These studies and earthquake epicenters [*Hill et al.*, 1990] define roughly vertical planes beneath the major strike-slip faults. The maximum depth of seismicity ranges from 10 to 22 km in different portions of the study area. The lower crust is well constrained only by the Loma Prieta, BASIX, and San Francisco Peninsula refraction data. These studies indicate the presence of a 6-10 km thick, high-velocity, mafic layer at the base of the crust [*Page and Brocher*, 1993; *Brocher et al.*, 1994; *Holbrook et al.*, 1996]. The crust in the study area thickens eastward from 20 km to 28 km [*Brocher et al.*, 1999].

2. Data

The 130 by 220 km study area for the tomographic inversion is shown in Figures 1 and 2. The *X-Y* coordinate system was derived from a transverse Mercator projection with a central longitude of 122°W. The point $X = 30$ km, $Y = 0$ km was tied to 37°N, 122°W, and the coordinate system was rotated 35° about this point. Depth Z is given relative to sea level, with stations and earthquakes above sea level located at negative depths.

Earthquakes and stations from the NCSN were obtained from the Northern California Earthquake Data Center, maintained by the USGS and the University of California, Berkeley [*Romanowicz et al.*, 1994]. Earthquakes from 1968 through June 1995 were sorted for quality using the criteria below, which are stricter than for most California tomography studies. Hypocenters in the catalogue are computed using one-dimensional (1-D) velocity models with linear velocity gradients. Ten different velocity models are used in different portions of the study area [*Oppenheimer et al.*, 1993]. In the catalogue the velocity model is assigned based on the earthquake location, allowing different velocity models for the same station but compensating with station corrections.

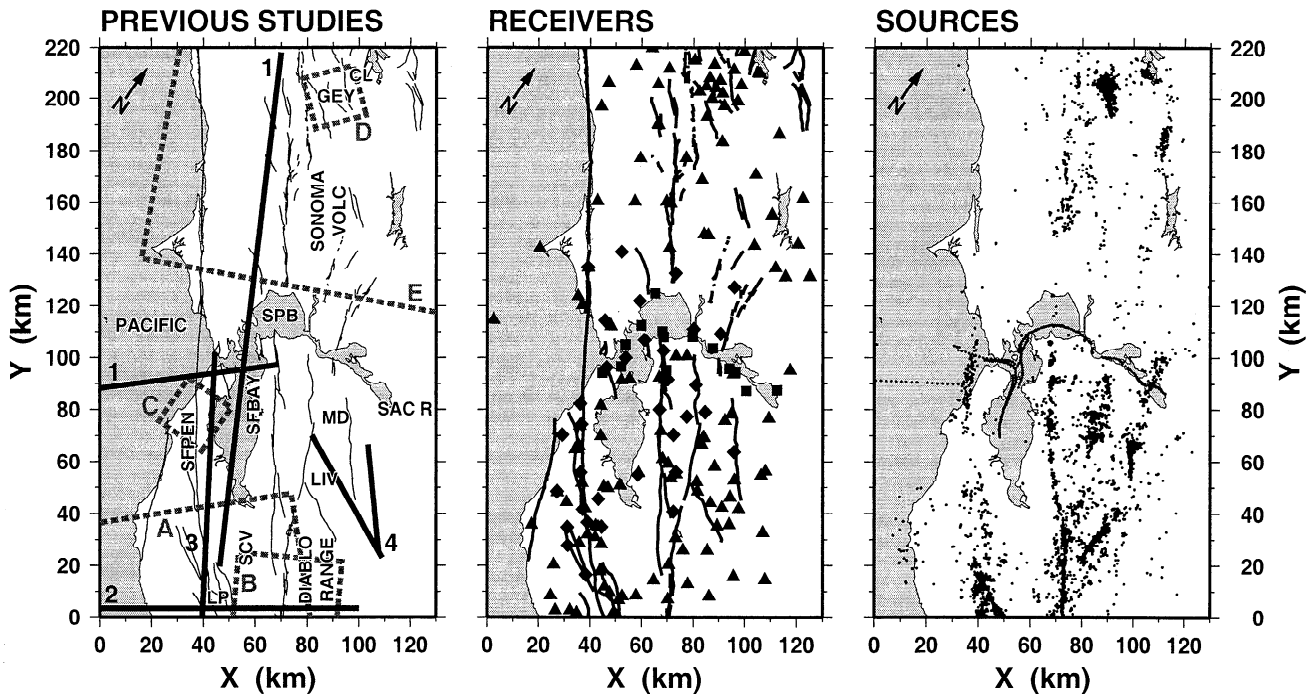

Figure 2. Maps of the study area (Figure 1). (left) Previous seismic refraction (thick solid lines) and tomography (dashed boxes) studies. Faults are indicated by thin lines. Seismic refraction studies, in order of the quality of constraints at the crustal scale, are 1, *Holbrook et al.* [1996]; 2, *Page and Brocher* [1993]; 3, *Catchings and Kohler* [1996]; and 4, *Meltzer et al.* [1987]. Other refraction profiles exist but constrain only 1-D or very shallow structure within the study area. Seismic tomography studies, in some cases representative of several studies at the same location (see text), are A, *Eberhart-Phillips and Michael* [1998]; B, *Michael* [1988]; C, *Parsons and Zoback* [1997]; D, *Julian et al.* [1996]; and E, *Stanley et al.* [1998]. Although the model of *Stanley et al.* [1998] covers a large portion of the study region, no detailed images of the crust were published south of $Y = 180$. Place names are SFBAY, San Francisco Bay; SFPEN, San Francisco Peninsula; SPB, San Pablo Bay; SAC R, Sacramento River; SCV, Santa Clara Valley; LIV, Livermore Valley; MD, Mount Diablo; LP, Loma Prieta; GEY, The Geysers; CL, Clear Lake volcanic field; SONOMA VOLC, Sonoma volcanic field. (middle) Receivers and (right) sources used in this study. Temporary BASIX stations (squares) recorded the air gun shots in the waterways (regular lines of sources). Earthquake epicenters are mainly distributed along the major faults (thick lines, center), with significant clusters at The Geysers and Loma Prieta. NCSN stations which recorded earthquakes are indicated by triangles and those which recorded both earthquakes and air gun shots are indicated by diamonds.

Travel time picks from the catalogue were not included in the 3-D tomographic inversion if their quality was poor enough that they were not considered in the catalogue hypocenter computation. Picks were also discarded if the travel time misfit from the catalogue hypocenter was >0.5 s. Earthquakes were used only if the magnitude was ≥2.0, the catalogue hypocentral error estimates were <2 km in depth and <1 km horizontally, and the root-mean-square (rms) hypocentral travel time misfit was <0.2 s. Finally, each earthquake had to be recorded with acceptable quality on at least 10 stations within the study area. Rays were traced to a maximum epicentral distance of 90 km to minimize use of the mantle refraction phase. This distance is based upon the cross-over distance of 90-100 km in BASIX refraction data. Figure 2 shows the 160 stations and 7742 earthquakes used in the inversion, yielding a total of 231,396 earthquake travel times.

In addition to the earthquake data, wide-angle refraction data from the BASIX survey were used in the inversion. An air gun array was fired every 50 m along overlapping ship tracks in the Pacific Ocean, along SFBay, and up the waterways to the Sacramento River delta (Figure 2). The shots were recorded in an off-line geometry at 14 temporary seismograph stations [*Brocher and Moses*, 1993] and 34 NCSN stations [*Brocher and Pope*, 1994] (Figure 2). These data were picked at a small, regularly spaced subset (259) of the air gun shots, adding 2874 controlled-source travel times to the inversion. Coherency of the first arrival in a receiver gather from spatially nonaliased sources improved the quality of the picks. Since the travel times represent only a subset of the redundant information and, unlike the earthquakes, the source locations are known, the BASIX data were given 10 times weighting in the inversion.

The source and receiver coverage (Figure 2) directly control the spatial resolution of the velocity model that can be determined through tomographic inversion. The majority of the earthquakes lie along the major strike-slip faults and the NCSN station spacing mimics the seismicity. The BASIX data complement the earthquakes by providing sources off the coast and between the faults and receivers on sediments near the waterways. The BASIX data also provide important short-offset data to constrain the shallow velocity structure. Earthquake and station coverage, and hence ray coverage, is

very dense from San Francisco Peninsula to the southeast quadrant of the study area (Figure 2). Average station spacing is 10-15 km in these regions. Except for the Rogers Creek Fault, coverage is much sparser north of SFBay. The northern San Andreas Fault has almost no seismicity and the station spacing is 20-30 km (Figure 2). A local cluster of stations records very high seismicity at shallow depth at The Geysers at the northern end of the study area. There is almost no coverage west of the coast or in the Great Valley east of the study area. The spatial resolution of the velocity model correlates with these variations in ray coverage.

3. Inversion Algorithm

The data were inverted using the travel time tomography algorithm of *Hole* [1992], extended to allow the determination of earthquake hypocenters. First-arrival travel times and rays in 3-D media are computed using a finite difference solution to the eikonal equation [*Vidale*, 1990]. A well-documented problem with the finite difference algorithm for large, sharp velocity contrasts was corrected without sacrificing the algorithm's superior accuracy or speed [*Hole and Zelt*, 1995]. Eikonal solvers are much faster than two-point ray tracing for a given model complexity and travel time accuracy, significantly reducing the computation time and thereby allowing a much higher spatial resolution to be considered. True first arrivals are always found, regardless of model complexity. Travel times for a source are calculated everywhere within the velocity model, thus times at an arbitrarily large number of receivers are found simultaneously. Taking advantage of the reciprocity of travel times, computational savings are derived by shooting at the relatively small number of seismograph stations and treating the earthquakes and air gun shots as receiver sites.

A linearized velocity inversion is performed through simple backprojection [*Hole*, 1992]. Times and rays are recomputed and inverted in an iterative nonlinear scheme that allows for arbitrarily complex velocity structure and ray paths. Nonlinear inversion becomes more important as the spatial resolution of the model improves [*Hole*, 1992]. While backprojection inversion converges slowly relative to other matrix inversion techniques and thus requires more forward modeling steps, the effect reduces as the spatial resolution of the model improves. Slow convergence also provides advantages in user control as described below.

The choice of model parameterization can strongly affect the type of model produced by an inversion. In the case of gridded models, both the size and the location of grid cells can affect the solution [e.g., *Toomey and Foulger*, 1989]. The use of large grid cells can create well-resolved model parameters since many rays penetrate each cell but at the expense of spatial resolution. More important, artifacts can be created by forcing the model to have the shape of the parameterization. *Toomey and Foulger* [1989] discuss this issue in terms of fidelity, the ability of the parameterization to reproduce expected structure. Alternatively, it can be considered as an issue of spatial resolution at each point in the subsurface, where the spatial resolution should be centered at the point of interest rather than being forced to lie in predefined cells. The chosen parameterization should be capable of resolving the smallest objects that can be detected by the data. For these reasons, it is preferable to overparameterize the model with small grid cells and to stabilize the inversion through explicit smoothing. This increases the computational cost of the inversion.

A few modifications were made to the velocity tomography procedure to allow greater flexibility in the model smoothing. The slowness (inverse velocity) correction, δu, at each grid node is computed during each backprojection as the average of the contributions from rays in the neighboring grid cells:

$$\delta u(\text{grid point}) = \sum_{\text{cells}} \sum_{\text{rays}} \frac{\delta t_{\text{ray}}}{l_{\text{ray}}} ,$$

where δt is the travel time misfit and l is the total length of the ray in the previous model [*Hole*, 1992]. The algorithm was modified to allow this average to occur within a larger 3-D rectangular box centered at the grid point of interest and containing numerous grid cells. The slowness correction is calculated at every grid point, even though the volume affecting each grid point is larger than the grid spacing. The use of small grid cells and larger backprojection boxes is analogous to a moving average filter, except it is nearby data constraints, not model results, that are being averaged. Once the slowness correction is determined for every grid point, this model perturbation is smoothed with a 3-D moving average filter of arbitrary size. Then the velocity model is updated, and new rays and travel times are computed for the next iteration. The size of both smoothing operations is controlled separately in each 3-D grid direction. These two types of smoothing have complementary attributes. The large backprojection box is good at averaging constraints from many rays, while the moving average filter is good at interpolating into ray gaps and extrapolating toward zero at the edges of ray coverage. Tests show that a combination of the two operations with similar physical dimensions produces the best results. Excellent fidelity is maintained by the small grid spacing, which allows anomalies to be located correctly, while spatial resolution and inversion stability are directly controlled by the size of the smoothing operators.

When the size of the smoothing operators gets very large, the slowness correction is close to linear over several grid points. To save the substantial computation time of the 3-D smoothing filters, the two operations can be performed at a regularly sampled subset of the grid nodes and subsequently interpolated to all the nodes. This temporary regridding operation makes the inversion grid sparser than the forward modeling grid, saving computation time but sacrificing fidelity. It is used only when the inversion is looking for very large scale structure, while the forward modeling algorithm requires small grid cells for accuracy. In practice, the regridding is chosen conservatively so that the regridded smoothing operations remain greater than 10 grid nodes in size in each direction.

The velocity tomography algorithm was extended to allow the quasi-simultaneous inversion for earthquake source parameters. The hypocenter locations and times in the NCSN earthquake catalogue contain errors because they are determined using simple, 1-D velocity models that cannot represent more complex structure. The effects of an incorrect velocity model upon earthquakes located using such a model are well documented [e.g., *Giardini*, 1992]. Similarly, velocity tomography that fixes the hypocenters at the catalogue locations is prone to systematic bias and artifacts [e.g., *Thurber*, 1992]. This issue is usually addressed by performing a simultaneous inversion for both velocity and

hypocenter parameters. However, this too fixes the trade-off between velocity and hypocenters. Some simultaneous inversion algorithms do not provide full flexibility to explore this highly nonlinear trade-off, and many users neglect to explore the trade-off. The new algorithm allows exploration of the full spectrum of possibilities between fixed hypocenters and fixed velocity model.

A linearized inversion for earthquake source parameters is performed assuming a fixed velocity model. Within a given velocity model a small perturbation in the hypocenter location (X, Y, Z) and time T will produce a small change in the observed travel time t_i for station i:

$$\left.\frac{\partial t_i}{\partial X}\right|_{\bar{\mathbf{R}}_0} \delta X + \left.\frac{\partial t_i}{\partial Y}\right|_{\bar{\mathbf{R}}_0} \delta Y + \left.\frac{\partial t_i}{\partial Z}\right|_{\bar{\mathbf{R}}_0} \delta Z + \delta T = \delta t_i \ ,$$

where the partial derivatives are evaluated at the unperturbed hypocenter:

$$\bar{\mathbf{R}}_0 = (X_0, Y_0, Z_0, T_0) \ .$$

Since the stations are used as sources and the finite difference algorithm calculates times to all grid nodes, the derivatives can be easily obtained as finite differences by calculating the average travel time gradient across the grid cell containing the earthquake. The travel time itself is found by trilinear interpolation within the grid cell. The travel time gradient and misfit for each earthquake is calculated for a given station and appended to a file. After calculations for all stations the file is sorted by earthquake. The set of linear equations for an individual earthquake is then inverted using singular value decomposition. Assuming many stations recorded the earthquake, this produces a leastsquares correction for the earthquake location and time. If fewer than four stations recorded the earthquake or if the solution is very poorly determined as indicated by small singular values, the earthquake is discarded from the inversion. Station corrections are not used because they represent near-station geology. Since the finite difference travel time algorithm allows sources and receivers anywhere within the model, true station elevations are used, and remaining station static shifts are attributed to velocity near the station.

If the wave fronts computed from every station are planar across the distance that the hypocenter is moved, then the linearized equation above is exact. For larger hypocenter perturbations an iterative nonlinear scheme is used, forward modeling between iterations. Synthetic data tests in moderately complex 3-D velocity models show that two to four iterations, depending upon the accuracy of the initial hypocenters, are sufficient to produce the correct solution. If the forward modeling results (the travel time at every grid node calculated from every station) are saved in a file, the forward modeling step in the nonlinear hypocenter inversion consists of simply sampling the travel time and travel time gradient at the hypocenter from the most recent iteration. This algorithm has the potential to provide a fast earthquake locator in complex 3-D velocity models by computing travel times and storing them on computer disk. The computational expense is 4 bytes of disk space per grid node per seismograph station. *Moser et al.* [1992] and *Wittlinger et al.* [1993] use similar methods to provide statistics on the hypocenter.

The linearized inversions for velocity and hypocenter are usually combined into a single matrix inversion solved directly or through parameter separation [e.g., *Thurber*, 1983]. If the convergence toward the iterative nonlinear solution is sufficiently slow, then alternating between solving the linearized velocity and linearized hypocenter inversions provides an effective approximation of simultaneous linearized inversion, which is itself only an approximation of the coupled nonlinear problem. Even with known shot locations, an intentionally slowed convergence toward the velocity model has advantages. A very stable procedure utilizes extremely large smoothing operators during the early iterations to first model large-scale velocity structure, then progressively smaller smoothing is used to approach the final detailed solution. This approach minimizes dependence on the initial velocity model and pushes the model toward an overall smooth solution, similar to the strategy of *Kissling et al.* [1994]. Interleaving iterations which invert for hypocenters allows the hypocenters to track the velocity model as it evolves. The relative rates of velocity and hypocenter convergence can be directly controlled, allowing exploration of the nonlinear trade-off between the two parameters. This allows the inversion algorithm to perform less as a black box and more as a tool to explore the full range of nonunique solutions. Stable inversion strategies and an understanding of nonuniqueness become increasingly important as data sets improve and allow more detailed spatial resolution. Tests with the SFBay area data demonstrate the value of this approach.

4. Velocity Model and Hypocenters

The velocity model was gridded at a 1-km spacing within the 130 x 220 km study area of Figure 1, from -3 to 30 km below sea level. Plate 1 shows horizontal slices at selected depths through the preferred final model. Note that both the absolute velocity and the velocity range represented by the color scale change with depth. Vertical slices through the catalogue and final velocity models are shown in Plate 2. The final hypocenters are shown in Plates 1 and 2 and Figure 3. The starting velocity model was a 1-D constant gradient (Figure 4) and the starting hypocenter locations were from the NCSN catalogue. The smoothing strategy for the velocity perturbation started with extremely large filters and gradually reduced their size as the model converged (preferred column of Table 1). Smoothing was uniform throughout the model. A hypocenter inversion iteration was performed after every third velocity iteration. The final model is the result of 18 velocity iterations interleaved with 6 hypocenter iterations and a final smoothing size of 12 x 12 x 2 km. The final rms travel time misfit is 144 ms (Table 1).

The strategy used to create the final model was thoroughly tested. The goal of the inversion was to produce a robust model that contains minimum structure. The preferred convergence scheme (Table 1) was designed to converge slowly with gradually decreasing smoothing operators so that subsequent iterations have the best "starting" model [e.g., *Kissling et al.*, 1994]. Tests show that slow convergence with the large smoothing operators minimizes dependence on the starting model and prevents small-scale anomalies caused by erroneous initial ray paths. Additional iterations with the final or smaller smoothing improved the spatial resolution and data fit but began to show bull's-eye artifacts. These artifacts were due to the overmodeling of data noise in poorly constrained portions of the model and were avoided at the expense of limiting spatial resolution in better constrained regions. The X and Y smoothing sizes were kept equal to

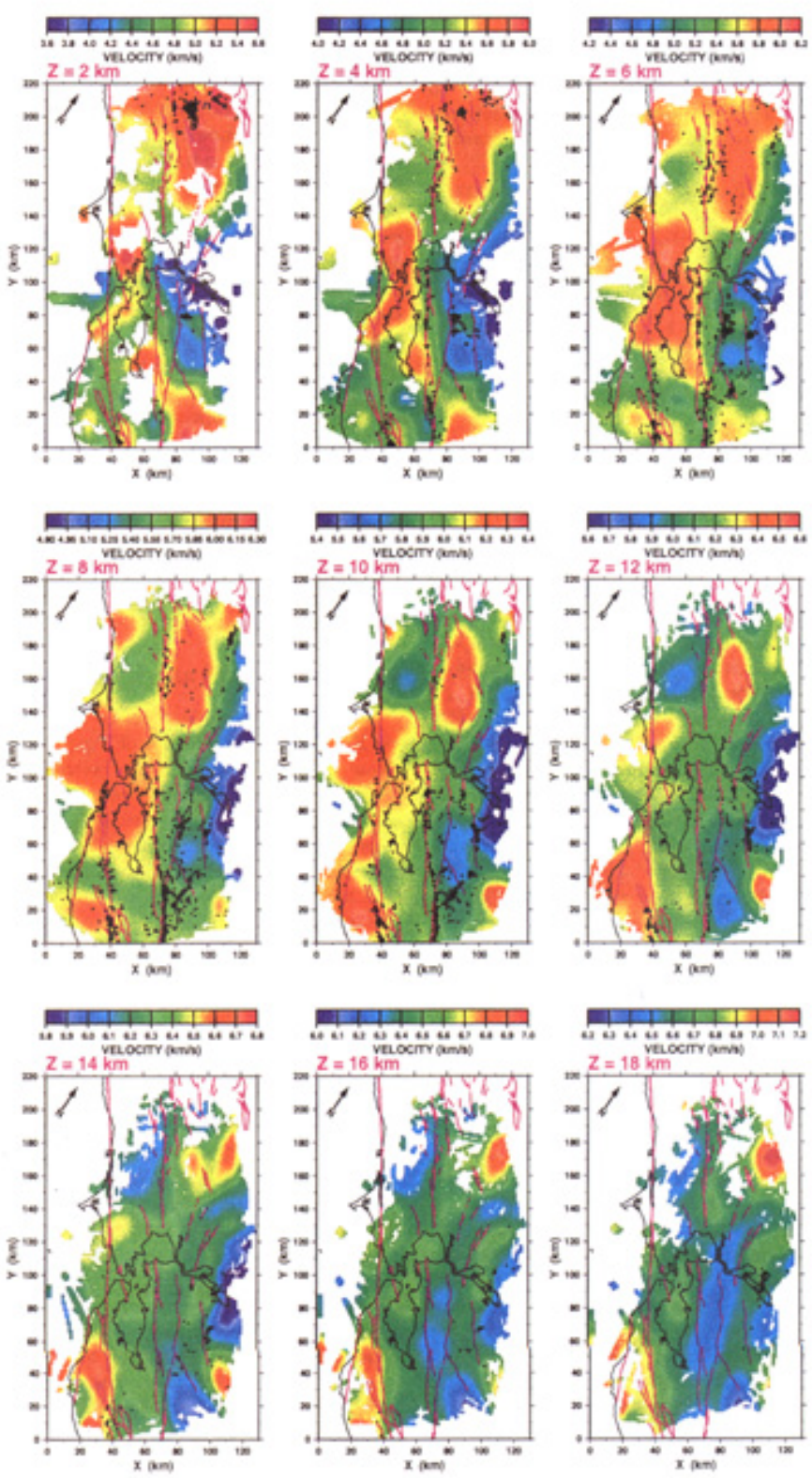

Plate 1. (opposite) Horizontal slices through the preferred 3-D seismic velocity model. The depth of the slice is labeled above each plot. Note that the absolute velocity and range of velocity both change for each slice, as indicated in the color scales. Grid points >1 km from a ray are not shown. Earthquake hypocenters within 1 km of the slice are included as black dots. The surface locations of major faults are shown in magenta.

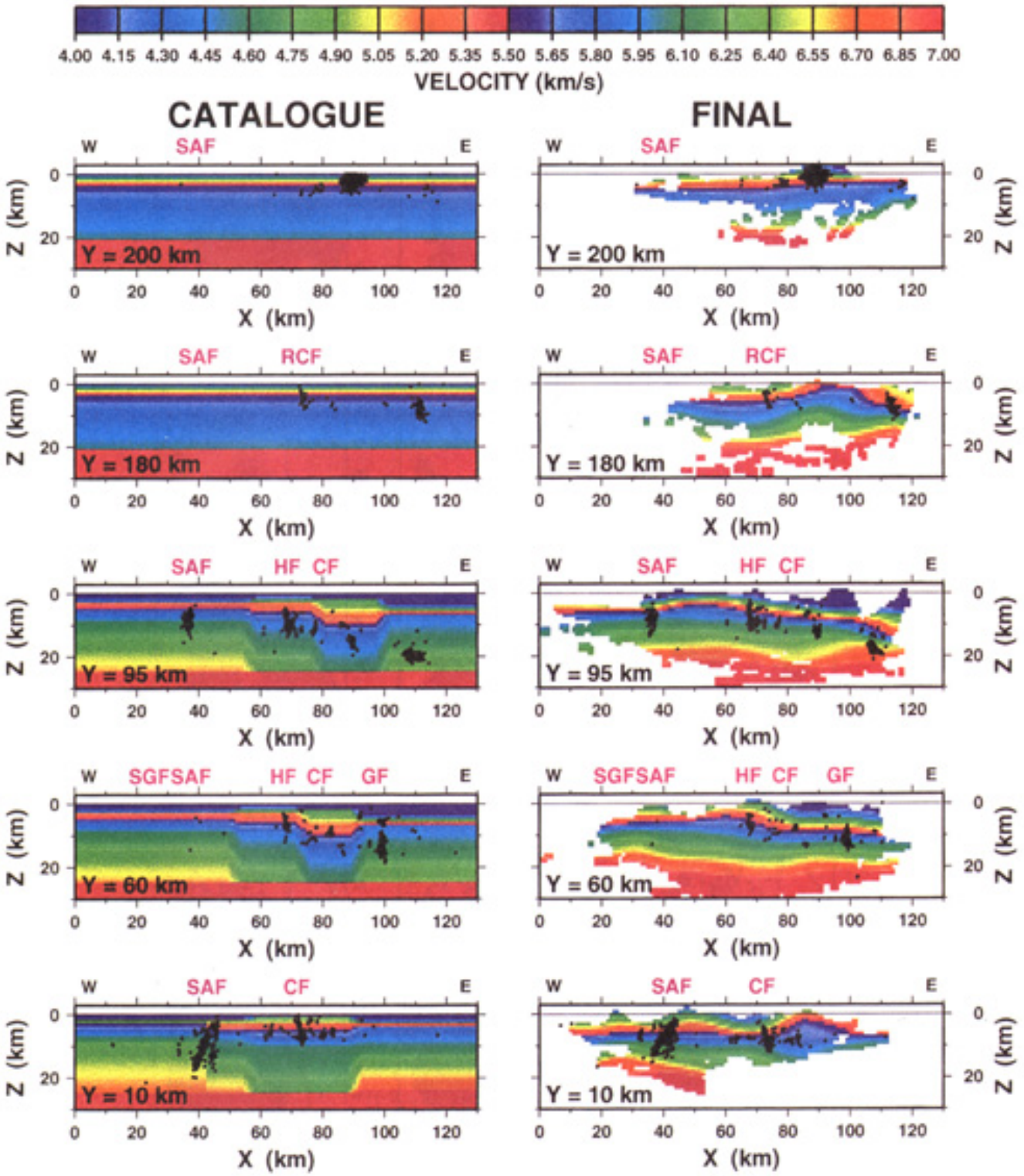

Plate 2. Selected across-strike vertical slices through the 3-D model at locations indicated in the lower left corner and in Figure 3. (left) The velocity models used to locate earthquakes in the NCSN catalogue. A single 1-D model plus station corrections is used for each earthquake regardless of station location. (right) The preferred final velocity model. Grid points more than 1 km from a ray are not shown. The catalogue and final hypocenters within 5 km of each slice are included as black dots. The surface locations of faults are labeled as in Figure 1.

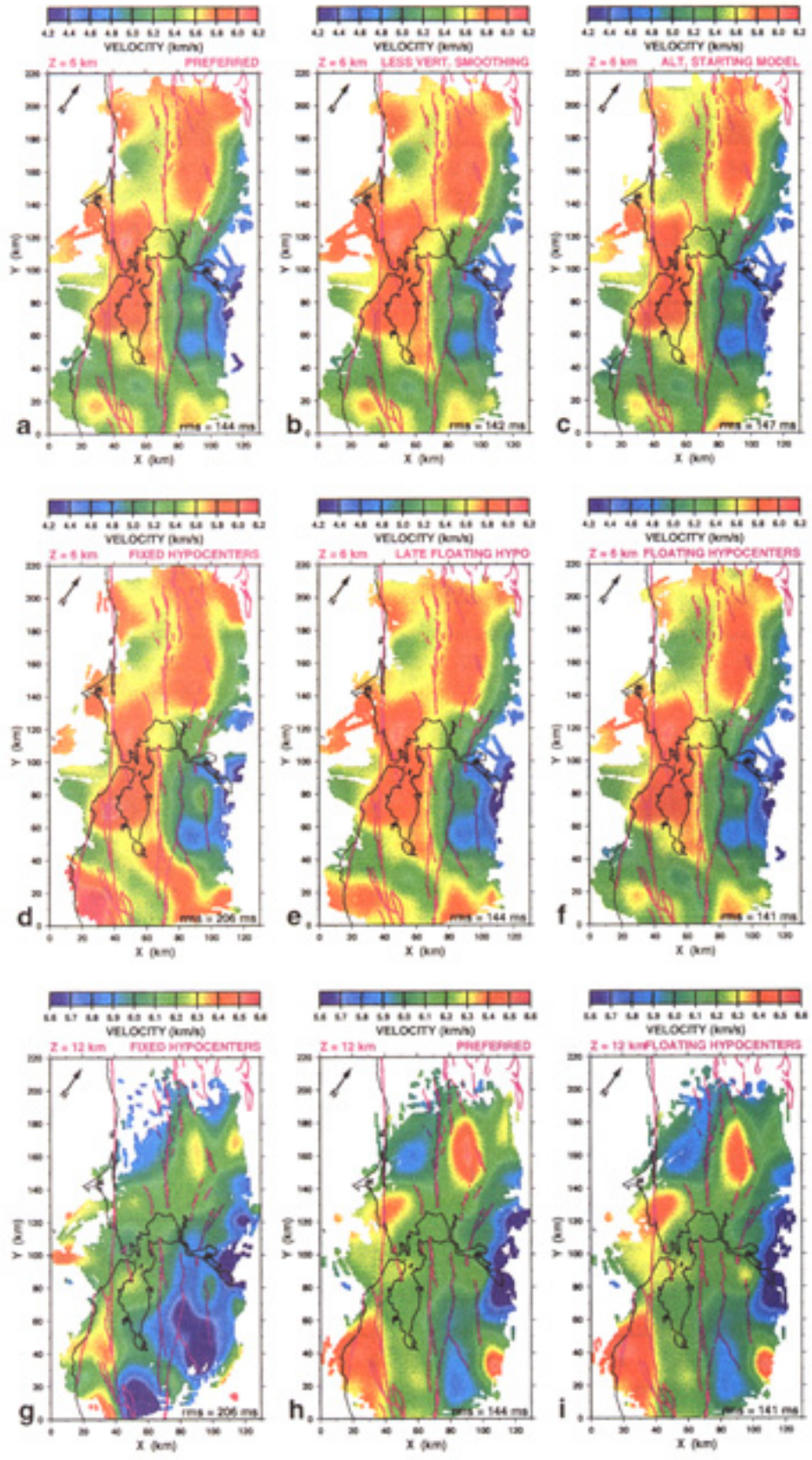

Plate 3. (opposite) Horizontal slices through several 3-D velocity models used to test the inversion results, plotted as in Plate 1 but without earthquakes. Table 1 shows convergence and smoothing schemes for the various models. Slices are at 6 km (Plates 3a-3f) and 12 km (Plates 3g-3i) depth for comparison. (a, h) Preferred model. (b) Model with less vertical smoothing. (c) Model derived from the alternate starting model (Figure 4). (d, g) Inversion with hypocenters fixed at the catalogue locations. (c) Inversion with earthquakes fixed for several iterations, then included in the inversion. (f, i) Inversion where the hypocenters closely track changes in the velocity model. The rms travel time misfit for each model is labeled in the lower right corner of the slice.

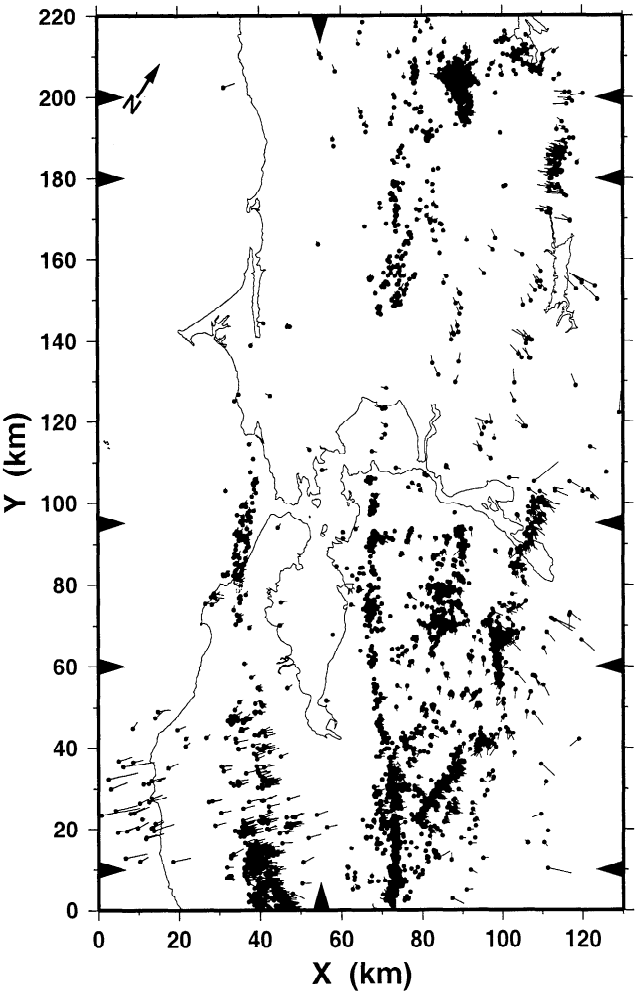

Figure 3. Earthquakes used in the tomographic inversion. Dots indicate the final epicenters from the preferred tomography model. Thin lines connect the final epicenters to the NCSN catalogue epicenters. Most earthquakes were relocated <2 km. Arrowheads indicate the locations of the cross sections shown in Plate 2 and Figure 5.

avoid bias, even though greater along-strike continuity might be expected. The ratio of horizontal to vertical smoothing was more important. If the vertical smoothing is too small, alternating layers of high and low velocity can be produced that are not required by the data. A vertical smoothing that is too large prevents sharp delineation of real boundaries such as the base of basins. A model derived with a smaller vertical smoothing (parentheses in Table 1; Plate 3b) provided very little improvement in depth resolution, suggesting that sedimentary basement cannot be better resolved by the data without a priori assumptions of a sharp velocity contrast. Such an assumption is not necessarily correct where "basement" is Cretaceous sediment [e.g., *Meltzer et al.*, 1987].

One of the disadvantages of linearized inversion schemes is that the result often depends upon the starting model. The relatively slow convergence with gradually decreasing smoothing greatly reduces this dependence. Four different 1-D starting models were tested using the preferred convergence scheme, two with constant velocity gradients (Figure 4) and two with a gradient which decreased with depth. Since the goal was a minimum-structure model constrained only by the data, results of previous studies were not incorporated in the starting model. Linearized tomography that applies spatially smooth perturbations to the starting model cannot get rid of higher-frequency structure imposed by a starting model. This includes the high-frequency component of broadband structure, such as discontinuities. The constant gradient models are thus preferred. The results can be independently compared to previous models. The starting model with the lower gradient produced a final model with an average 1-D velocity ~0.1 km/s slower (Figure 4). These two starting models have very different initial velocity gradients, which results in very different initial ray coverage and application of velocity perturbations. However, lateral and vertical velocity contrasts, relative earthquake locations, and the data misfits in the two final models are very similar (Plates 3a and 3c). Since these two starting models bracket the final average gradients, they can probably be considered end-members. The difference in average velocity is due to a trade-off between hypocenter depth and velocity. The average hypocenter depth was 0.57 km shallower in the slower model. Either of these models is acceptable by any measurable criterion, so the preference for the faster model is arbitrary.

Similarly, the slow convergence scheme is insensitive to reasonable errors in the initial hypocenters because the earthquakes are relocated in the velocity model before detailed velocity structure is allowed. The trade-off between hypocenters and velocity was explored using different relative rates of hypocenter and velocity convergence (Table 1). Plates 3d and 3g show results with fixed hypocenter locations (Table 1), pushing the travel time misfits into the velocity model. The final data misfit is much larger than the misfits for the inversions that relocate the hypocenters. Parts of the fixed-hypocenter velocity model mimic the various 1-D models used to locate the earthquakes, but other parts are inconsistent with the 1-D models. For example, large-amplitude anomalies at 12 km depth (Plate 3g) contain unrealistic velocities and do not correlate well with surface geology. Earthquake tomography without hypocenter inversion is generally considered incorrect because artifacts can be created in the velocity model [e.g., *Thurber*, 1992]. Plates 3f and 3i allowed the hypocenters to float by using a large number of hypocenter iterations (Table 1). Since the hypocenter-only linearized inversion converges in significantly fewer iterations than the velocity-only linearized inversion, the hypocenters are completely relocated before the velocity evolves far from the starting model. This scheme continuously relocates the earthquakes as the velocity model evolves, pushing as much of the travel time misfit as possible into the hypocenters. While this may be optimum for minimizing velocity structure, it is at the possible expense of scatter or bias in the hypocenters. The true solution probably lies between these models. The preferred solution (Plate 1) allows more of the travel time misfit to be assigned to the velocity model but is close enough to the floating hypocenter model that it is virtually independent of the starting hypocenters. An alternative scheme fixes the hypocenters during determination of the large-scale structure, trusting the catalogue to be close to correct at these scales, then subsequently floating the hypocenters (Table 1 and Plate 3e). The range of models produces very similar large scale

Table 1. Tomography Convergence Schemes and RMS Travel Time Misfits

Smoothing Size	Fixed Hypocenter (Plates 3d and 3g)	Preferred (Plates 1, 3a, and 3h)	Less Vertical Smoothing (Plate 3b)	Alternate Starting Model (Plate 3c)	Late Floating Hypocenter (Plate 3e)	Floating Hypocenter (Plates 3f and 3i)
	620	620	620	516	620	620
100 x 100 x 20 (100 x 100 x 12)	vel, vel, vel	vel, vel, vel, hypo	vel, vel, vel, hypo	vel, vel, vel, hypo	vel, vel, vel	vel, hypo, vel, hypo, vel, hypo
	365	252	246	250	365	260
70 x 70 x 14 (70 x 70 x 8)	vel, vel, vel	vel, vel, vel, hypo	vel, vel, vel, hypo	vel, vel, vel, hypo	vel, vel, vel	vel, hypo, vel, hypo, vel, hypo
	319	238	232	240	319	242
50 x 50 x 10 (50 x 50 x 6)	vel, vel, vel	vel, vel, vel, hypo	vel, vel, vel, hypo	vel, vel, vel, hypo	vel, vel, vel	vel, hypo, vel, hypo, vel, hypo
	297	223	218	227	297	224
30 x 30 x 6 (30 x 30 x 4)	vel, vel, vel	vel, vel, vel, hypo	vel, vel, vel, hypo	vel, vel, vel, hypo	vel, hypo, vel, hypo, vel, hypo	vel, hypo, vel, hypo, vel, hypo
	269	200	197	203	203	200
20 x 20 x 4 (20 x 20 x 2)	vel, vel, vel	vel, vel, vel, hypo	vel, vel, vel, hypo	vel, vel, vel, hypo	vel, hypo, vel, hypo, vel, hypo	vel, hypo, vel, hypo, vel, hypo
	238	174	170	176	174	172
12 x 12 x 2 (12 x 12 x 2)	vel, vel, vel	vel, vel, vel, hypo	vel, vel, vel, hypo	vel, vel, vel, hypo	vel, hypo, vel, hypo, vel, hypo	vel, hypo, vel, hypo, vel, hypo
	206	144	142	147	144	141

vel, linearized velocity inversion iteration; hypo, linearized hypocenter (earthquake location and time) inversion iteration. Rays and times are computed at every iteration. Misfits are in ms. Smoothing sizes in parentheses are for Plate 3b only.

structure above 10 km depth, but contains some variation in details. All of the inversions with hypocenter relocation produce similar data misfits. The trade-off between hypocenters and velocity is most pronounced at the edges of the model region, followed by depths at and below the deepest earthquakes.

Spatial resolution determined using the linearized matrix can provide false confidence, particularly when implicit constraints are placed on the model through a coarse parameterization. "Checkerboard" tests using a realistic model provide estimates of the spatial resolution for the full nonlinear and nonunique problem. Synthetic travel time data were created for the sources and receivers of Figure 2 using the final preferred hypocenters and a checkerboard velocity model composed of 2-D ±0.4 km/s sinusoids added to the 1-D average of the final preferred model (thick solid line in Figure 4). Data sets were computed for 10, 15, 20, and 30 km half-wavelength anomalies and each was inverted using the preferred convergence scheme. The starting model was the catalogue hypocenters and the preferred 1-D velocity model (thin solid line in Figure 4). The 10-km checkerboard could only be resolved in portions of the model volume through extra iterations with a smaller smoothing. Although the model can be resolved locally to 10 km or better, the regional model cannot without allowing overmodeling artifacts, such as streaking along rays. The 15-km checkerboard is moderately well resolved south of the Rogers Creek Fault, from the San Andreas Fault to the Greenville Fault and at depths less than about 6 km (Plate 4a). A few extra iterations improve the poor image of Plate 4a, indicating that this resolution is truly but barely achieved. The 20-km checkerboard is well resolved through most of the region to 10 km depth and is moderately resolved in the central and southern regions to about 14 km depth (Plates 4b and 4c). Anomalies that are 30 km in size are resolved to about 18 km depth (Plate 4d). In all of the checkerboard tests, extra iterations increased the amplitude of the moderately well resolved checkerboard pattern toward the true value. This suggests that the model of Plate 1 may underestimate the amplitude of velocity variations that are spatially too small to be well resolved. The very small 1-km grid spacing ensures that the anomalies are located properly and the model has excellent fidelity. All tests indicate that the preferred velocity model (Plate 1) is a smooth version of the true structure, preventing overinterpretation.

Tests using different starting models and vertical smoothing indicate that the vertical resolution is ~2 km above 12 km depth and 3-4 km below 14 km depth. While the upper 2 km of the model is subject to the near-station trade-off of velocity versus thickness, short-offset BASIX refraction data eliminate this effect locally and reduce it regionally. The alternate starting model indicates about a 0.1 km/s trade-off with hypocenter depth (Figure 4). However, the slopes of the

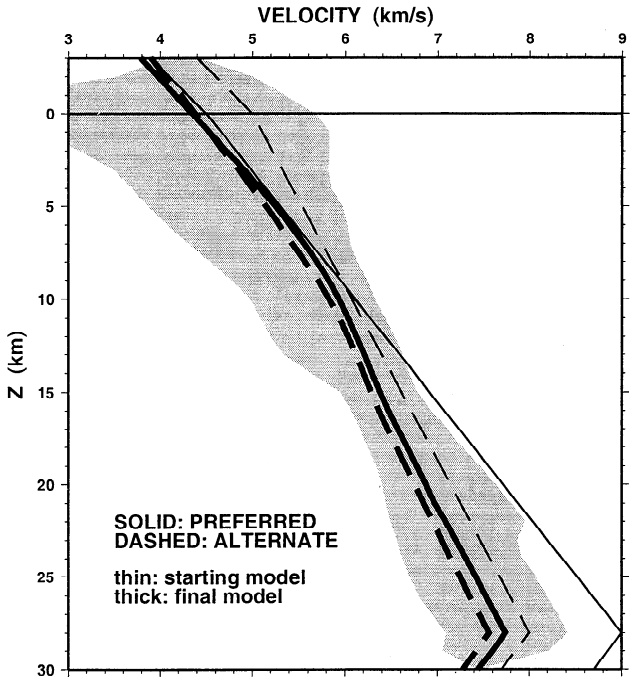

Figure 4. One-dimensional starting (thin lines) and final average (thick lines) velocity models for the preferred (solid lines; Plate 1) and alternate (dashed lines; Plate 3c) inversions. Shading indicates the range in velocity in the preferred final model. Most of the 3-D model lies much closer to the 1-D average than the extreme values shown.

average 1-D velocity profiles for the two models have maxima, minima, and inflection points at the same depths. This suggests that features in the velocity model are subject to a global shift of <1 km in depth. At and below the deepest earthquakes, at 10 km depth north of SFBay and 14-16 km elsewhere, there exists a larger trade-off between hypocenter depth and velocity. Averaging over the spatial resolution described above, the velocity values throughout the model are accurate to ~0.1 km/s.

Figure 5 compares the BASIX 2-D refraction model along SFBay (Figure 2) [*Holbrook et al.*, 1996] with the preferred 3-D tomography model. The tomography algorithm smooths the vertical discontinuities in the refraction model. Owing to the small shot aperture and limited number of receivers, the spatial resolution of the refraction model is similar to the 3-D model in the upper crust. The refraction analysis allowed a higher spatial resolution in the upper 3 km in order to match shot and receiver travel time delays. BASIX wide-angle reflections from the lower crust provide an average velocity of 6.1 km/s between 8 and 15 km depth, in good agreement with the low-gradient region (5.8–6.4 km/s) observed in the tomography model (Figures 4 and 5). Subsurface sources in the 3-D data better constrain laterally varying structure at these depths. The refraction model utilized reflections and mantle refractions to provide information about the lower crust. These depths are not well constrained by the 3-D first-arrival data, but velocities near 7 km/s are indicated in both models. Overall, there is good agreement between the two models.

5. Interpretation

Lateral variations in the velocity model are strongest in the near surface, where the color scale of Plate 1 covers the broadest range. The shallow velocity structure correlates well with the surface geology and the isostatic residual gravity (Plate 5). The isostatic residual is computed by the removal of crustal thickness variations from the Bouguer gravity, assuming isostatic compensation of elevation. In the SFBay area it provides a good measure of the shallow geology and is useful where the geology is hidden by a thin Cenozoic sedimentary cover.

West of the San Andreas Fault, most of the Salinian terrane is overlain by Tertiary sediments. The tomography model at 2 km depth indicates high velocity and the residual gravity

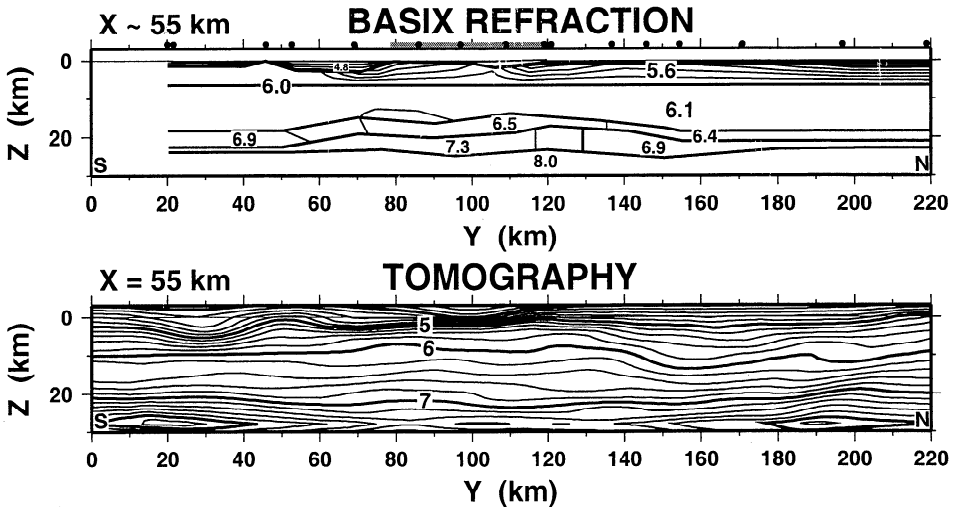

Figure 5. Comparison of the along-strike BASIX 2-D refraction velocity model from *Holbrook et al.* [1996] with the corresponding vertical slice through the preferred 3-D model. Labels are in km/s, and the contour interval is 0.2 km/s. Discontinuities and integer velocity values are shown as thicker lines. BASIX airgun shots and receivers are indicated by the shaded line and solid circles, respectively. The BASIX profile is slightly oblique to the tomography cross section (Figure 2) but is very close to the section where it is best constrained between $Y = 50$ and 160 km. The two models are similar within the spatial resolution of the two techniques.

reaches maxima at the few Salinian outcrops (Plate 5). Onshore, the velocity model exceeds 4.8 km/s by 4 km depth, and the gravity is relatively high, suggesting that the sedimentary rocks are at most a few kilometers thick. West of the coast, deeper Cenozoic basins are indicated by poorly constrained low velocities. Similar to refraction [*Page and Brocher*, 1993; *Holbrook et al.*, 1996] and tomography [*Eberhart-Phillips and Michael*, 1998] models in the area, the average Salinian velocity increases to 6.0 km/s at ~8 km depth and 6.3 km/s at 12 km (Plate 1).

Between the San Andreas and the Hayward-Rogers Creek Faults, outcrops of the Franciscan terrane correlate well with higher gravity and faster shallow velocity (Plate 5). Most of the Cenozoic sediment under SFBay is only a few hundred meters thick [e.g., *Holbrook et al.*, 1996], and the velocity quickly rises to 4.8-5.3 km/s, typical of shallow Franciscan rocks. The gravity and velocity both indicate the presence of deeper basins under southeastern SFBay and the Santa Clara Valley. Basin thickness estimated from the velocity model is ~5 km beneath the Santa Clara Valley, in agreement with *Michael* [1988] and ~3 km beneath SFBay. The average velocity increases to 6.0 km/s at ~10 km depth and 6.2 km/s at 12 km (Plate 1), similar to previous results [*Holbrook et al.*, 1996; *Eberhart-Phillips and Michael*, 1998; *Stanley et al.*, 1998]. Velocities ~0.3 km/s lower are observed north of Y = 145 km, where the ray coverage provides relatively poor constraints. The lower velocity could be due to thin Tertiary sediments at the surface (Plate 5) and to younger Oligocene to Eocene Franciscan rocks which outcrop north of Y = 175 km [*Jennings*, 1977] and may underthrust older rocks farther south.

East of SFBay, outcrops of the Franciscan terrane produce shallow velocity and gravity highs at Mount Diablo and in the Diablo range (Plate 5). At shallow depths the Great Valley Sequence and Cenozoic sediments are slower than the Franciscan terrane. Very low velocity and gravity indicate deep Cenozoic basins beneath eastern San Pablo Bay (~4 km thick), the Livermore Valley (~6 km), the Sacramento River, and the Great Valley at the eastern edge of the study area (Plate 5). Depending upon diagenetic and tectonic history, it can be difficult to distinguish the Franciscan, Great Valley, and Cenozoic sediments at depth based upon velocity alone [*Meltzer et al.*, 1987], and hence depth to the underlying Franciscan terrane is not well defined. However, using 5.0 km/s as the criterion, the top of the Franciscan terrane lies at ~4 km depth west of the Calaveras Fault and ~6 km depth surrounding Mount Diablo east of the Calaveras Fault (Plate 1). A depth of about 6 km to Franciscan terrane beneath the Livermore Valley agrees with previous shallow refraction estimates [*Meltzer et al.*, 1987].

Very low velocity persists to a depth of at least 14 km beneath the Sacramento River delta at the eastern edge of the model (Plates 1 and 2), where the Sacramento Basin extends westward from the Great Valley into the Coast Ranges (Plate 5). While some vertical smearing exists at the edge of ray coverage, the model indicates that Great Valley sediments exist to a depth of at least 12 km. Such a great depth to Great Valley basement is supported by BASIX refraction data and is suggested by trends in surrounding areas [*Wentworth et al.*, 1995, *Brocher et al.*, 1999]. These deep sediments are not included in the velocity model used to locate the catalogue seismicity. Catalogue hypocenters indicate that the easternmost SFBay area seismicity extends to more than 22 km depth (Plate 2, Y = 95 km), some of the deepest seismicity in California's strike-slip system [*Hill et al.*, 1990]. The tomography model relocates these earthquakes to depths <20 km at the sharp western boundary of the basin (Plates 1 and 2).

East of the Rogers Creek Fault, the surface geology is complex, comprising slivers of the Franciscan terrane, Great Valley Sequence, ultramafic ophiolite associated with the faulted terrane boundary, and Cenozoic volcanism (Plate 5). The gravity data correlate with trends in the geology but the velocity model is uniformly fast. The seismic station coverage is relatively sparse in most of this region, and the spatial resolution is larger than the geologic units, so the model may be averaging the effects of the shallow igneous rocks. Relatively high seismic velocity persists to at least 11 km depth beneath the Sonoma volcanic field but not beneath The Geysers and the Clear Lake volcanic field farther north (Plate 1), similar to the less well resolved deep results of *Stanley et al.* [1998]. The velocity beneath the Sonoma volcanics reaches 6.0 km/s at about 7 km depth and is 6.4 km/s at 12 km depth. These values are higher than normal for the Franciscan terrane and are presumably due to felsic intrusion or metamorphism associated with the volcanism. The velocity is too low for extensive mafic intrusion in the upper crust. No large low-velocity body exists in the midcrust beneath The Geysers region, in agreement with other recent data contradicting earlier studies which had suggested a large midcrustal magma chamber [*Stanley et al.*, 1998].

The most striking feature of the velocity images of Plate 1 is the strong correlation between lateral contrasts in seismic velocity and the major strike-slip faults. These correlations persist vertically beneath the surface locations of the faults to the maximum depths constrained by the model. In the upper crust the San Andreas Fault is manifested as small velocity contrasts that vary along strike. Beginning at ~9 km depth and persisting to the maximum depth of ray coverage, the Salinian terrane to the west of the San Andreas Fault is faster than the Franciscan terrane to the east (Plate 1). This contrast is most evident in the southern portion of the study region, including the 1989 Loma Prieta epicentral region (X < 20 km). North of SFBay, the Rogers Creek Fault and related along-strike faults form the western boundary of the high-velocity effects of the Cenozoic volcanism (Plate 1). This velocity contrast persists where Franciscan rocks are on both sides of the faults at depth, perhaps because of the younger age of the Franciscan terrane to the west at this latitude. The Hayward Fault is marked by a strong velocity contrast in the upper crust, with higher velocity to the west (Plate 1). Near the surface, this is due to the boundary between the Franciscan terrane and the Great Valley Sequence. The velocity contrast becomes more subtle but persists through the middle crust, where the Franciscan terrane is presumed to exist on both sides of the fault. Both the velocity contrast and seismicity step east from the Hayward to the Calaveras Fault along the Mission Fault (Y = 40-50 km). To the north, the velocity contrast across the Hayward Fault steps east to line up with the Rogers Creek fault, but at 6-9 km depth the step appears to be ~15 km south of its surface location in San Pablo Bay. Faults farther east of SFBay bound low-velocity Cenozoic basins at shallow depths and correlate roughly with velocity anomalies at greater depth (Plate 1).

The resolution of the velocity model decreases rapidly below the deepest earthquakes at ~10 km depth north of SFBay, 15 km depth near the bay, and 20 km depth at the edge of the Great Valley. The lower crust in the region is a high-velocity mafic layer, producing a strong, sharp velocity

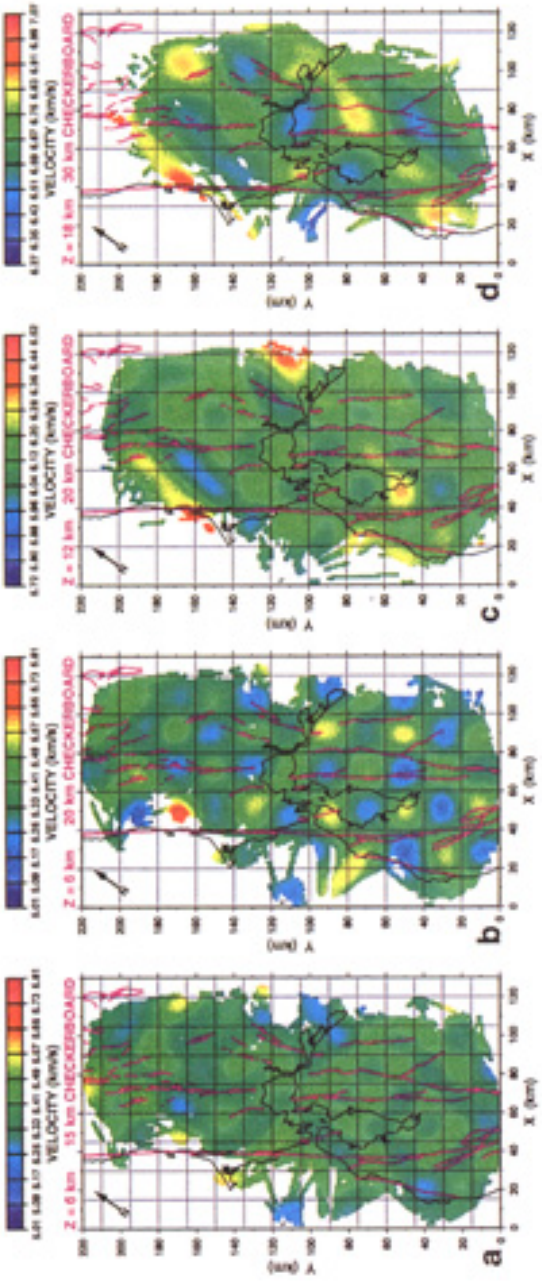

Plate 4. Horizontal slices through 3-D velocity models derived from synthetic data, plotted as in Plate 1. Data were derived from plus-minus checkerboard patterns added to a 1-D velocity model (see text). The size of the checkerboards in each inversion is labeled and shown with a thin grid of lines. Slices in Plates 4a, 4c, and 4d were intentionally chosen at depths (labeled) where the velocity anomalies were barely resolved and the amplitudes underestimated; shallower slices were always better resolved.

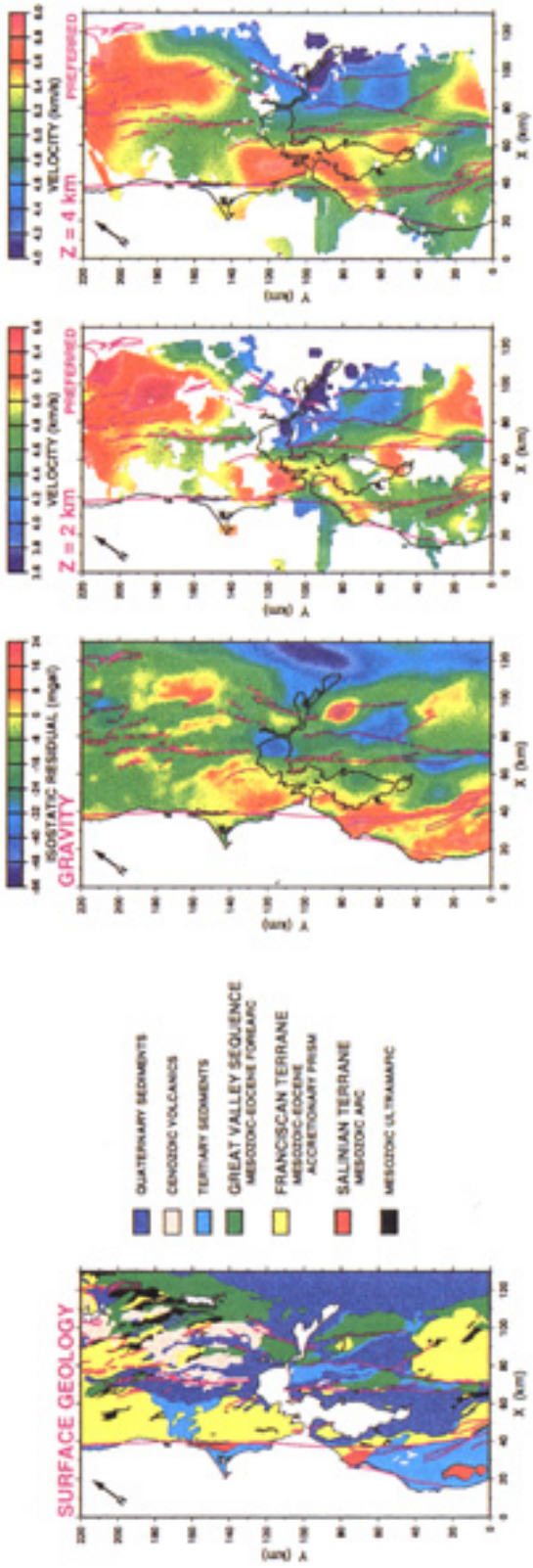

Plate 5. Comparison of surface geology [*Jennings*, 1977], isostatic residual gravity [*Snyder et al.*, 1981], and shallow slices through the preferred 3-D velocity model (Plate 1). Faults are shown in magenta.

contrast with the overlying rocks [*Brocher et al.*, 1994]. Refraction data indicate that the top of the mafic layer gets deeper from west to east and is at ~15 km depth beneath SFBay [*Holbrook et al.*, 1996; *Brocher et al.*, 1999]. Since the sharp nature of the boundary cannot be resolved by the first arrival data, particularly considering the depth trade-off for the deep hypocenters, the velocity contrast is vertically smoothed by the tomography algorithm. There was no attempt to incorporate a more realistic sharp velocity contrast. An inflection point at the start of an increasing velocity gradient occurs at 14 km depth in the average 1-D velocity model (Figure 4), indicating the shallowest effects of the mafic layer. The velocity increases to values >6.6 km/s, indicative of a mafic lithology, at ~14 km depth to the west of the San Andreas Fault (Plate 1). The velocity decreases eastward, with 6.6 km/s encountered at ~17 km depth beneath SFBay and 19 km depth east of the Hayward Fault.

While the spatial resolution of the velocity model in the lower crust is poor, lateral variations correlate with the surface faults (Plate 1). Since the top of the mafic layer is a strong velocity contrast and has been smoothed vertically, the lateral velocity contrasts across the faults most likely indicate changes in the depth of the top of the mafic layer. Lateral velocity variations within the lower crust are possible, but variations in the depth of the top of the lower crust will produce a stronger effect. A third possibility is that the lateral variations are due to the eastward deepening seismicity and resulting maximum depth of good resolution in the smoothed tomography results. Explicit incorporation of a priori sharp boundaries in the inversion may allow discrimination between these models. If either of the geologic interpretations is true, it would support recent evidence that suggests the strike-slip faults cut through the mafic layer to the Moho [*Holbrook et al.*, 1996; *Parsons*, 1998]. Faults that cut through the lower crust are inconsistent with tectonic models [*Page and Brocher*, 1993; *Bohannon and Parsons*, 1995] in which the mafic layer is oceanic crust attached to and moving with the Pacific plate. *Hole et al.* [1998] discuss the implications of such constraints on the evolution of the San Andreas Fault system. Unfortunately, resolution issues below the deepest earthquakes require the deep tomography observations to be treated as possible but not definitive.

Throughout the central portion of the study region, most earthquakes were relocated <2 km from the catalogue hypocenters (Figure 3 and Plate 2). The relocated seismicity on the active strike-slip faults defines a steeply dipping plane beneath the surface expression of each fault. Large changes in the hypocenter locations along the edge of the Great Valley are due to poor station coverage and errors in the catalogue velocity models. Earthquakes near and west of the southern San Andreas Fault were relocated 2-4 km to the southwest and shallower. Previous tomography studies of the Loma Prieta aftershock zone incorporated refraction data and stations south of our study area [*Eberhart-Phillips and Michael*, 1998] and hence are superior in this area at the edge of our model. Our Loma Prieta aftershocks dip at an angle consistent with previous studies (Plate 2, $Y = 10$ km). The southern Calaveras Fault is the only other major fault with a nonvertical plane of seismicity (Plate 2). Similar to the results of *Michael* [1988], the relocated earthquakes define a plane with a steep eastward dip ~10° shallower than in the catalogue.

Throughout the study area, no earthquakes occur in regions with velocity >6.3 km/s (Plates 1 and 2). All of the inversion tests produced this result, usually with a maximum velocity of 6.2 km/s. This result persists despite the trade-off between the depth of the deepest earthquakes and the velocity at that depth. This is most likely an indication that Franciscan rocks exist to depths greater than the brittle-ductile transition and always have velocities <6.3 km/s [*Holbrook et al.*, 1996; *Hole et al.*, 1998]. The maximum depth of seismicity in the southern half of the study area (Plate 2) closely mimics the suggested depth to the top of the mafic layer in the lower crust. The top of the mafic layer should produce an increase in strength with depth [*Holbrook et al.*, 1996], so the base of seismicity must be thermally controlled within the Franciscan rocks rather than structurally controlled at the top of the mafic layer. The brittle-ductile transition occurs at shallower depth north of SFBay.

6. Conclusions

Tomography has been used to invert earthquake and air gun travel time data in the SFBay area for 3-D seismic velocity and hypocenters. Nonuniqueness was explored in a new inversion algorithm by varying the starting model, the relative rates of velocity and hypocenter inversion, and the smoothing scheme. The model is consistent with surface geology and gravity data and allows extrapolation of surface structure to depth. Lateral velocity contrasts exist at all depths vertically beneath the major strike-slip faults, indicating that the faults penetrate most of the crust. The 3-D velocity model provides an improved understanding of the distribution of the major geologic units in the SFBay area.

Several smaller regions within the study area contain sufficient seismicity and stations to resolve finer-scale structure. Previous tomography studies at the southern end of our study region provide higher-resolution images near major faults (Figure 2). However, these studies do not include regionally recorded seismicity and thus do not constrain well the structure farther from the faults, which in turn affects the near-fault image. The regional model described here should be used as a starting point to improve such local tomography studies. This approach was employed by *Parsons and Zoback* [1997] and *Stanley et al.* [1998] (Figure 2), who used regional models to better constrain local studies.

The model also has practical applications toward understanding earthquake hazards in this densely populated area. Improved studies of past and future seismicity in a realistic 3-D model are crucial to an understanding of fault behavior. Strong ground motions from major earthquakes in the SFBay area depend strongly upon the 3-D seismic velocity structure of the crust [e.g., *Catchings and Kohler*, 1996; *Stidham et al.*, 1999]. Finally, constraining the extent and rheological properties of the main geological units will aid modeling of the strain behavior of the crust and interactions between SFBay area faults [e.g., *Reasenberg and Simpson*, 1992; *Burgmann*, 1997]. The incorporation of the new seismic velocity model will improve research in these important topics.

Acknowledgments. This research received support from the U.S. Geological Survey National Earthquake Hazards Reduction Program. We thank Bill Ellsworth for conversations about earthquake tomography procedures. Barry Zelt, David Snyder, David Oppenheimer, Andrew Michael, and an anonymous person provided valuable reviews that improved this manuscript. The project was initiated while J.A.H. was working at Stanford University with S.L.K. and at the USGS in Menlo Park with Walter Mooney and Gary Fuis.

References

Bohannon, R.G., and T. Parsons, Tectonic implications of post-30 Ma Pacific and North American relative plate motions, *Geol. Soc. Am. Bull., 107*, 937-959, 1995.

Brocher, T.M., and M.J. Moses, Onshore-offshore wide-angle seismic recordings of the San Francisco Bay area seismic imaging experiment (BASIX): The five-day recorder data, *U.S. Geol. Surv. Open File Rep., 93-0276*, 1993.

Brocher, T.M., and D.C. Pope, Onshore-offshore wide-angle seismic recordings of the San Francisco Bay area seismic imaging experiment (BASIX): Data from the Northern California seismic network, *U.S. Geol. Surv. Open File Rep., 94-0156*, 1994.

Brocher, T.M., J. McCarthy, P.E. Hart, W.S. Holbrook, K.P. Furlong, T.V. McEvilly, J.A. Hole, and S.L. Klemperer, Seismic evidence for a lower-crustal detachment beneath San Francisco Bay, California, *Science, 265*, 1436-1439, 1994.

Brocher, T.M., U.S. ten Brink, and T. Abramovitz, Synthesis of crustal seismic structure and implications for the concept of a slab gap beneath coastal California, *Int. Geol. Rev., 41*, 263-274, 1999.

Burgmann, R., Active detachment faulting in the San Francisco Bay area?, *Geology, 25*, 1135-1138, 1997.

Catchings, R.D., and W.M. Kohler, Reflected seismic waves and their effect on strong ground shaking during the 1989 Loma Prieta, California, earthquake, *Bull. Seismol. Soc. Am., 86*, 1401-1416, 1996.

Eberhart-Phillips, D., Three-dimensional velocity structure in northern California Coast Ranges from inversion of local earthquake arrival times, *Bull. Seismol. Soc. Am., 76*, 1025-1052, 1986.

Eberhart-Phillips, D., and A.J. Michael, Seismotectonics of the Loma Prieta, California, region determined from three-dimensional *Vp*, *Vp/Vs*, and seismicity, *J. Geophys. Res., 103*, 21,099-21,120, 1998.

Foxall, W., A. Michelini, and T.V. McEvilly, Earthquake travel time tomography of the southern Santa Cruz Mountains: Control of fault rupture by lithological heterogeneity of the San Andreas fault zone, *J. Geophys. Res., 98*, 17,691-17,710, 1993.

Giardini, D. (ed.), Lateral heterogeneity and earthquake location, *Phys. Earth Planet. Int., 75*, 198 pp., 1992.

Hill, D.P., J.P. Eaton, and L.M. Jones, Seismicity, 1980-86, in *The San Andreas fault system, California*, edited by R.E. Wallace, *U.S. Geol. Surv. Prof. Pap., 1515*, 115-151, 1990.

Holbrook, W.S., T.M. Brocher, U.S. ten Brink, and J.A. Hole, Crustal structure of a transform plate boundary: San Francisco Bay and the central California continental margin, *J. Geophys. Res., 101*, 22,311-22,334, 1996.

Hole, J.A., Nonlinear high-resolution three-dimensional seismic travel time tomography, *J. Geophys. Res., 97*, 6553-6562, 1992.

Hole, J.A., and B.C. Zelt, 3-D finite-difference reflection traveltimes, *Geophys. J. Int., 121*, 427-434, 1995.

Hole, J.A., B.C. Beaudoin, and T.J. Henstock, Wide-angle seismic constraints on the evolution of the deep San Andreas plate boundary by Mendocino triple junction migration, *Tectonics, 17*, 802-818, 1998.

Jennings, C.W., Geologic map of California, Calif. Div. of Mines and Geol., Sacramento, 1977.

Jennings, C.W., Fault activity map of California and adjacent areas, Calif. Div. of Mines and Geol., Sacramento, 1994.

Julian, B.R., A. Ross, G.R. Foulger, and J.R. Evans, Three-dimensional seismic image of a geothermal reservoir: The Geysers, California, *Geophys. Res. Lett., 23*, 685-688, 1996.

Kissling, E., W.L. Ellsworth, D. Eberhart-Phillips, and U. Kradolfer, Initial reference models in local earthquake tomography, *J. Geophys. Res., 99*, 19,635-19,646, 1994.

Meltzer, A.S., A.R. Levander, and W.D. Mooney, Upper crustal structure, Livermore Valley and vicinity, California Coast Ranges, *Bull. Seismol. Soc. Am., 77*, 1655-1673, 1987.

Michael, A.J., Effects of three-dimensional velocity structure on the seismicity of the 1984 Morgan Hill, California, aftershock sequence, *Bull. Seismol. Soc. Am., 78*, 1199-1221, 1988.

Moser, T.J., T. van Eck, and G. Nolet, Hypocenter determination in strongly heterogeneous Earth models using the shortest-path method, *J. Geophys. Res., 97*, 6563-6572, 1992.

Oppenheimer, D., F. Klein, J. Eaton, and F. Lester, The Northern California Seismic Network bulletin January-December 1992, *U.S. Geol. Surv. Open File Rep., 93-578*, 1993.

Page, B.M., and T.M. Brocher, Thrusting of the Central California margin over the edge of the Pacific Plate during the transform regime, *Geology, 21*, 635-638, 1993.

Page, B.M., G.A. Thompson, and R.G. Coleman, Late Cenozoic tectonics of the central and southern Coast Ranges of California, *Geol. Soc. Am. Bull., 110*, 846-876, 1998.

Parsons, T., Seismic-reflection evidence that the Hayward fault extends into the lower crust of the San Francisco Bay area, California, *Bull. Seismol. Soc. Am., 88*, 1212-1223, 1998.

Parsons, T., and M.L. Zoback, Three-dimensional upper crustal velocity structure beneath San Francisco Peninsula, California, *J. Geophys. Res., 102*, 5473-5490, 1997.

Reasenberg, P.A., and R.W. Simpson, Response of regional seismicity to the static stress change produced by the Loma Prieta earthquake, *Science, 255*, 1687-1690, 1992.

Romanowicz, B., D. Neuhauser, B. Bogaert, and D. Oppenheimer, Accessing northern California earthquake data via internet, *Eos Trans. AGU, 75*, 257-260, 1994.

Romero, A.E., T.V. McEvilly, E.L. Majer, and D. Vasco, Characterization of the geothermal system beneath the northwest Geysers steam field, California, from seismicity and velocity patterns, *Geothermics, 24*, 471-487, 1995.

Snyder, D.B., C.W. Roberts, R.W. Saltus, and R.F. Sikora, The principal facts of 64, 026 gravity stations in the state of California, *U.S. Geol. Surv. Rep., PB82-168279* and *PB82-168287*, 1981.

Stanley, W.D., H.M. Benz, M.A. Walters, A. Villasenor, and B.D. Rodriguez, Tectonic controls on magmatism in The Geysers-Clear Lake region: Evidence from new geophysical models, *Geol. Soc. Am. Bull., 110*, 1193-1207, 1998.

Stidham, C., M. Antolik, D. Dreger, S. Larsen, and B. Romanowicz, Three-dimensional structure influences on the strong-motion wavefield of the 1989 Loma Prieta earthquake, *Bull. Seismol. Soc. Am., 89*, 1184-1202, 1999.

Thurber, C.H., Earthquake locations and three-dimensional crustal structure in the Coyote Lake area, central California, *J. Geophys. Res., 88*, 8226-8236, 1983.

Thurber, C.H., Hypocenter-velocity structure coupling in local earthquake tomography, *Phys. Earth Planet. Inter., 75*, 55-62, 1992.

Thurber, C.H., S.R. Atre, and D. Eberhart-Phillips, Three-dimensional *Vp* and *Vp/Vs* structure at Loma Prieta, California, from local earthquake tomography, *Geophys. Res. Lett., 22*, 3079-3082, 1995.

Toomey, D.R., and G.R. Foulger, Tomographic inversion of local earthquake data from the Hengill-Grensdalur central volcano complex, Iceland, *J. Geophys. Res., 94*, 17,497-17,510, 1989.

Vidale, J.E., Finite-difference calculation of traveltimes in three dimensions, *Geophysics, 55*, 521-526, 1990.

Walter, A.W., and W.D. Mooney, Crustal structure of the Diablo and Gabilan ranges, central California: A reinterpretation of existing data, *Bull. Seismol. Soc. Am., 72*, 1567-1590, 1982.

Warren, D.H., Seismic-refraction measurements of crustal structure near Santa Rosa and Ukiah, California, in *Research in The Geysers-Clear Lake Geothermal Area, Northern California*, edited by R.J. McLaughlin, and J.M. Donnelly-Nolan, *U.S. Geol. Surv. Prof. Pap., 1141*, 167-181, 1981.

Wentworth, C.M., G.R. Fisher, P. Levine, and R.C. Jachens, The surface of crystalline basement, Great Valley and Sierra Nevada, California: A digital map database, *U.S. Geol. Surv. Open File Rep., 95-96*, 1995.

Wittlinger, G., G. Herquel, and T. Nakache, Earthquake location in strongly heterogeneous media, *Geophys. J. Int., 115*, 759-777, 1993.

H. M. Benz, U.S. Geological Survey, P.O. Box 25046, MS 966, Lakewood, CO 80225. (benz@usgs.gov)

T. M. Brocher, U.S. Geological Survey, MS 977, 345 Middlefield Road, Menlo Park, CA 94025. (brocher@usgs.gov)

K. P. Furlong, Department of Geosciences, Pennsylvania State University, University Park, PA 16802. (kevin@geosc.psu.edu)

J. A. Hole, Department of Geological Sciences, Virginia Tech, 4044 Derring Hall, Blacksburg, VA 24061-0420. (hole@vt.edu)

S. L. Klemperer, Department of Geophysics, Stanford University, Stanford, CA 94305-2215. (sklemp@pangea.stanford.edu)

T. Parsons, U.S. Geological Survey, MS 999, 345 Middlefield Road, Menlo Park, CA 94025. (tparsons@usgs.gov)

(Received July 8, 1999; revised January 21, 2000;
accepted March 10, 2000.)